Multimodal Multiplexed Immunoimaging with Nanostars to Detect Multiple Immunomarkers and Monitor Response to Immunotherapies

Yu-Chuan Ou[†], Xiaona Wen[†], Christopher A. Johnson[‡,§], Daniel Shae[†], Oscar D. Ayala[⊥], Joseph A. Webb[†], Eugene C. Lin[▽,○,◆], Rossane C. DeLapp[•], Kelli L. Boyd[◇], Ann Richmond[‡,§], Anita Mahadevan-Jansen[⊥], Marjan Rafat[†,⊥,△], John T. Wilson[†,⊥,▲], Justin M. Balko[▲,#], Mohammed N. Tantawy[▽,○], Anna E. Vilgelm[‡,§,¶], Rizia Bardhan[†,⊥,○,‖,*]

[†]Department of Chemical and Biomolecular Engineering, Vanderbilt University, Nashville, Tennessee 37235, USA.
[‡]Tennessee Valley Healthcare System, Department of Veterans Affairs, Nashville, Tennessee 37212, USA.
[§]Department of Pharmacology, Vanderbilt University School of Medicine, Nashville, Tennessee 37232, USA.
[⊥]Department of Biomedical Engineering, Vanderbilt University, Nashville, Tennessee 37235, USA.
[▽]Radiology and Radiological Sciences, Vanderbilt University School of Medicine, Nashville, Tennessee 37232, USA.
[○]Vanderbilt University Institute of Imaging Science, Vanderbilt University School of Medicine, Nashville, Tennessee 37232, USA.
[◆]Department of Chemistry and Biochemistry, National Chung Cheng University, Chiayi 62106, Taiwan.
[•]Civil and Environmental Engineering, Vanderbilt University, Nashville, Tennessee 37235, USA.
[◇]Department of Pathology, Microbiology and Immunology, Vanderbilt University School of Medicine, Nashville, Tennessee 37232, USA.
[△]Department of Radiation Oncology, Vanderbilt University School of Medicine, Nashville, Tennessee 37232, USA.
[▲]Vanderbilt Center for Immunobiology, Vanderbilt University School of Medicine, Nashville, Tennessee 37232, USA.
[#]Department of Medicine, Vanderbilt University School of Medicine, Nashville, Tennessee 37232, USA.
[¶]Department of Pathology, Ohio State University, Columbus, Ohio 43210, USA.
[‖]Department of Chemical and Biological Engineering, Iowa State University, Ames, Iowa, 50012 USA.

[*]Corresponding Author
E-mail: rbardhan@iastate.edu

ABSTRACT

The overexpression of immunomarker programmed cell death protein 1 (PD-1) and engagement of PD-1 to its ligand, PD-L1, is involved in the functional impairment of cluster of differentiation 8 (CD8) T cells contributing to cancer progression. However, heterogeneities in PD-L1 expression and variabilities in biopsy-based assays render current approaches inaccurate in predicting PD-L1 status. Therefore, PD-L1 screening alone is not predictive of patient response to treatment, which motivates us to simultaneously detect multiple immunomarkers engaged in immune modulation. Here, we have developed a multimodal probe, immunoactive gold nanostars (IGNs), that accurately detects PD-L1^{+} tumor cells and CD8^{+} T cells simultaneously *in vivo*, surpassing the limitations of current immunoimaging techniques. IGNs integrate the whole-body imaging of positron emission tomography with high sensitivity and multiplexing of Raman spectroscopy, enabling the dynamic tracking of both immunomarkers. IGNs also monitor response to immunotherapies in mice treated with combinatorial PD-L1 and CD137 agonists, and distinguish responders from those nonresponsive to treatment. Our results showed a multifunctional nanoscale probe with capabilities that cannot be achieved with either modalities alone, allowing multiplexed immunologic tumor profiling critical for predicting early response to immunotherapies.

KEYWORDS

gold nanostar, immunoimaging, immunoPET, Raman spectroscopy, multiplexed detection, programmed cell death ligand 1, CD8

Upregulation of immune checkpoint PD-1 and subsequent binding of PD-1 to its ligand, PD-L1, impedes effector T cell function contributing to immunosuppression.[1, 2] Inhibition of the PD-1/PD-L1 axis with immunotherapies has transformed the therapeutic landscape for a broad array of cancers. However, despite the clinical efficacy of these agents, only a fraction of patients respond in most tumor types, and identifying patients likely to benefit from these therapies remains challenging.[3-5] Current predictive technologies rely on static measure of PD-L1 levels in biopsies which cannot adequately distinguish responders from nonresponders. This could be in part due to limited tissue sampling, or the spatial and temporal heterogeneity of PD-L1 among patients and even within the same patient's primary and metastatic lesions.[6, 7] Therefore, noninvasive molecular imaging is critical in the immunotherapy drug development pipeline for multiple reasons. First, this will allow accurate and dynamic measurement of PD-L1 status *in vivo* to identify patients who will respond to immunotherapies prior to treatment. Second, this will enable multiplexed recognition of other immunomarkers that show engagement of the immune tumor microenvironment (TME) to determine alternative therapies for patients who are nonresponsive to PD-L1 blockade. Third, this will establish end points for monitoring treatment efficacy early in the immunotherapy regimen and reflect the dynamic changes in immunomarker localization during therapeutic intervention.[8, 9]

Dynamic tracking of both PD-L1 and cytotoxic $CD8^+$ T cells *in vivo* is highly relevant to predict the complex interplay between the immune system and TME. The presence of $CD8^+$ T cells both within the tumor and at the invasive margin is a positive prognostic marker that demonstrates active engagement of antitumor immunity.[10, 11] Studies have shown that tumors that are infiltrated with $CD8^+$ T cells and simultaneously express PD-L1 are most likely to benefit from PD-L1 inhibitors.[12-14] Further, dynamic changes occur in both PD-L1 level in tumor cells and

$CD8^+$ T cells during treatment that cannot be captured by single biomarker imaging or by static measure of receptor status.[15, 16] The strong correlation between PD-L1 inhibition and activation of $CD8^+$ T cells motivates multiplexed detection of both markers to ultimately provide translatable methods for predicting clinical responses to immunotherapies.

In this work, we simultaneously detect PD-L1 and CD8 *in vivo* (Figure 1a) and monitor response to combinatorial immunotherapies with an innovative probe, immunoactive gold nanostars (IGNs), which combines positron emission tomography (PET) with surface-enhanced Raman spectroscopy (SERS). PET and SERS are complementary imaging techniques seamlessly integrated with IGNs, allowing depth-resolved whole-body imaging with PET to locate the macroscopic distribution of tumors to tissue depths of many centimeters. Multiplexed SERS is then followed to identify multiple immunomarkers that dynamically control local and systemic immunity in the TME. SERS, an optical technique, uses near-infrared (NIR) light to enhance the vibrational signal of Raman reporters, enables narrow spectral features amenable for multiplexing.[17] Gold nanostars are ideal for SERS because they have shown to amplify the signal of Raman molecules by $>10^9$ enabling enhanced spatiotemporal resolution *in vitro* and *in vivo*. [18-20] Here, we showed IGNs labeled with antibodies, Raman tags, and ^{64}Cu were targeted to melanoma tumors after systemic delivery *in vivo* in immunocompetent mice. IGNs detected both PD-L1 expressing cells and $CD8^+$ T cells in the TME with high sensitivity and specificity *via* ImmunoPET-SERS imaging. Further, IGNs effectively monitored response to immunotherapies in mice treated with a combination of anti-PD-L1 and anti-CD137 monoclonal antibodies (mAbs). CD137 is a costimulatory receptor expressed on activated T cells and shown to have synergistic therapeutic benefits with PD-L1 blockade.[21, 22] Both PET and SERS imaging with IGNs demonstrated an infiltration of $CD8^+$ T cells in BRAF-mutant YUMM 2.1 melanoma tumors after

immunotherapies that correlated well with a decrease in tumor growth. IGNs also distinguished responders from those nonresponsive to immunotherapies by examining NRAS-mutant YUMM 10.1 tumors that showed minimal change in PD-L1 and CD8 status post-treatment. We envision the findings of this work will catalyze a clinically translatable technology that will ultimately permit image-guided interventions ranging from noninvasive treatment planning to predicting therapeutic effectiveness and improve survival of cancer patients.

RESULTS AND DISCUSSIONS

Synthesis of Immunoactive Gold Nanostars (IGNs). Gold nanostars were synthesized with a biological buffer, HEPES (2-[4-(2-hydroxyethyl)piperazin-1-yl]ethanesulfonic acid), as previously described by our group.[23, 24] HEPES binds weakly to gold surfaces, offering a straightforward surface chemistry that allows covalent conjugation of both PET and Raman labels for imaging, and PEG ligands for biocompatibility to avoid recognition by the mononuclear phagocyte system (MPS). Multiplexed detection of both PD-L1 and CD8 was enabled by designing two sets of IGNs. To enable PD-L1 detection, nanostars were covalently conjugated with the Raman tag, para-mercaptobenzoic acid (pMBA), followed by covalent linking to anti-PD-L1 mAbs. Nanostars were then conjugated to chelators, (1,4,7,10-Tetraazacyclododecane-1,4,7,10-tetraacetic acid) (DOTA), and finally radiolabeled with ^{64}Cu (Figure 1b). We chose DOTA to chelate ^{64}Cu because this complex has already been utilized in patients for PET imaging[25-27] and is currently under numerous clinical trials (NCT03492762, NCT02827877, *etc*.). CD8 detection was facilitated by conjugating nanostars with anti-CD8 mAbs, the Raman tag 5,5-dithio-bis-(2-nitrobenzoic acid) (DTNB), and ^{64}Cu following a similar procedure. As PET cannot distinguish the signal between radiolabels, the two Raman tags allowed multiplexed detection of

the two immunomarkers. Covalent conjugation of IGNs with mAbs and chelated radiolabel was achieved *via* a bifunctional orthopyridyl-disulfide poly(ethylene glycol)-N-hydroxysuccinimide ester (OPSS-PEG-NHS) linker described in detail in methods and in supporting information (Scheme S1). Our previous work has shown this bifunctional linker not only provides stability to nanostars but also maintains bioactivity of the antibodies for successful *in vivo* detection.[28] PEG with this bifunctional linker stabilized the mAbs and DOTA, and thiols in the orthopyridyl disulphide (OPSS) group enabled covalent conjugation to nanostars surface. IGNs' size regime, 50 – 80 nm, (Figure 1c,d) is ideal for rapid accumulation in the TME, enabling longitudinal imaging and time-course study. Whereas this size can potentially limit efficient renal clearance of IGNs, recent studies has shown renal excretion of 50 nm mesoporous silica nanoparticles.[29] In addition, the size of IGNs should not impede their clinical translation, as micron-sized particles have been shown to filtrate through the kidneys in large animals and humans.[30, 31]

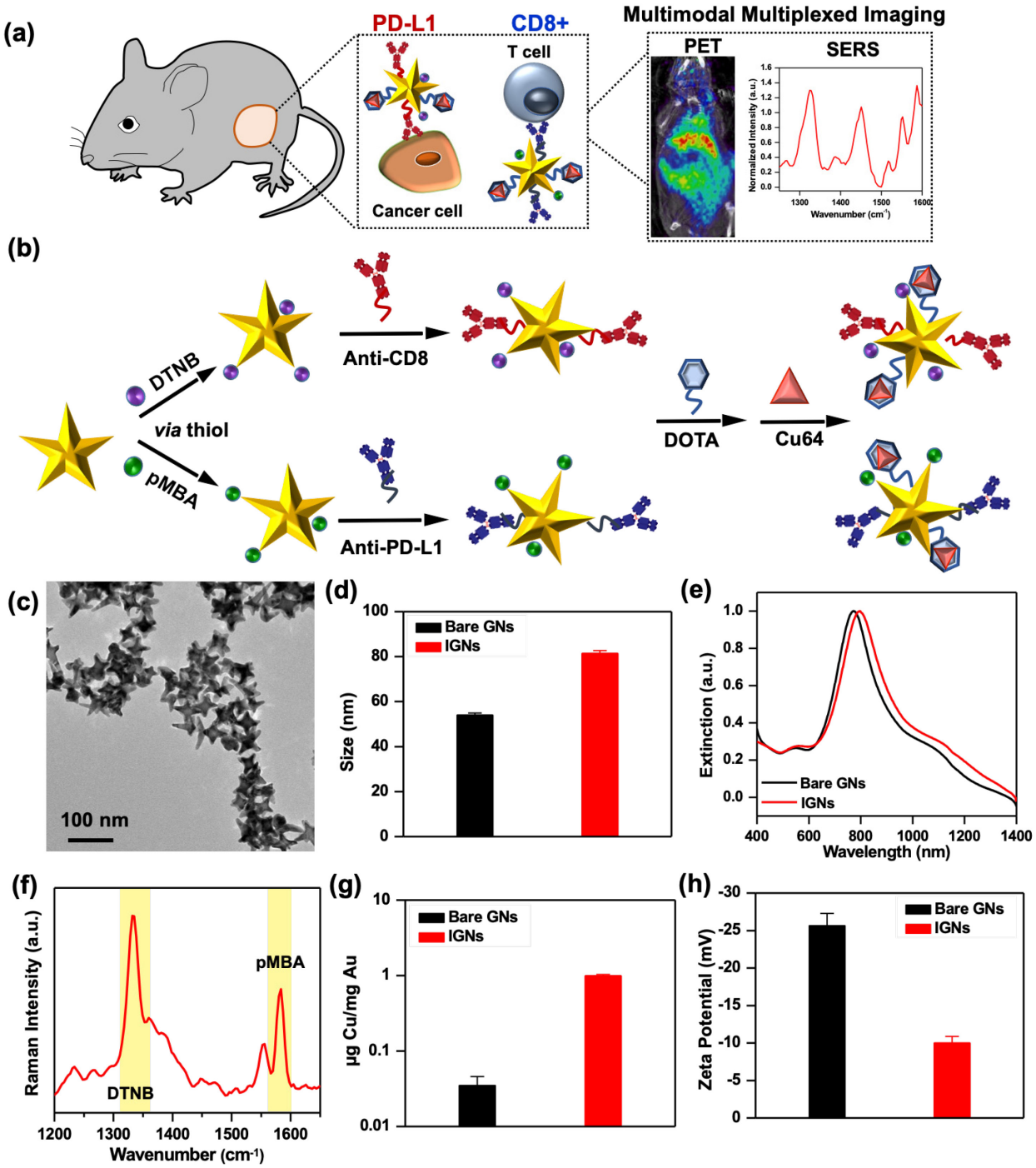

Figure 1. Design and Physicochemical Properties of IGNs. (a) Schematic representation of IGNs-mediated multimodal multiplexed ImmunoPET-SERS imaging to detect both PD-L1 expression and $CD8^+$ T cells in melanoma tumors. (b) IGNs design where gold nanostars were functionalized with Raman tags (pMBA or DTNB) *via* a thiol-Au reaction followed by conjugation with PEG stabilized antibodies (anti-PD-L1 or anti-CD8) and DOTA, and chelated with ^{64}Cu radiolabels. (c) Transmission electron micrograph of IGNs showing their star shape. (d) Hydrodynamic size of IGNs from dynamic light scattering. (e) Extinction spectra of bare gold nanostars and functionalized IGNs. (f) Raman spectra of a mixture of IGNs targeting CD8 and

PD-L1 *via* DTNB (1325 cm^{-1}) and pMBA (1580 cm^{-1}) tags, respectively; the signature peaks of the tags are highlighted. (g) Amount of Cu chelated per mg IGNs quantified *via* ICP-MS. (h) Zeta potential of the bare gold nanostars and IGNs showing surface charge.

The increase in nanostars size post-functionalization resulted in a ~30 nm red shift in their absorbance but remained resonant in the near-infrared (NIR) (Figure 1e). NIR light has a 1 – 3 cm penetration depth ideal for *in vivo* imaging.[32-34] The SERS spectra of an equimolar mixture of IGNs consisting of IGNs/anti-PD-L1/pMBA/^{64}Cu and IGNs/anti-CD8/DTNB/^{64}Cu showed the dominant peak of DTNB at 1325 cm^{-1} and pMBA at 1580 cm^{-1} (Figure 1f). We also validated cold Cu chelation to IGNs with inductively coupled plasma mass spectrometry (ICP-MS) and quantified 0.99 ± 0.04 μg Cu/mg Au in the presence of DOTA relative to 0.035 ± 0.02 μg Cu/mg Au for bare nanostars control, indicating successful radiolabeling of IGNs (Figure 1g). Further, zeta potential measurements (Figure 1f) confirmed PEG conjugation on IGNs results in near neutral surface charge in comparison to bare nanostars which have a negative charge. The stability of IGNs in both water and cellular media supplemented with serum was studied by examining the intensity and the full width at half maximum (FWHM) of the extinction spectra. The intensity remained unchanged (Figure S1a) and minimal broadening of extinction spectra was observed (Table S1) demonstrating IGNs did not flocculate over 4 days, which is the duration of longitudinal imaging in our study. In addition, the shelf life of IGNs was studied for 4 weeks. Aliquots of IGNs were dispersed in water, PBS, media, and media supplemented with serum. Minimal change was observed in the normalized extinction of IGNs (Figure S1b), and only slight (~1 – 6%) increase in FWHM (Table S2) over the course of 4 weeks. These results indicate IGNs have long shelf-life and good stability in the time frame studied.

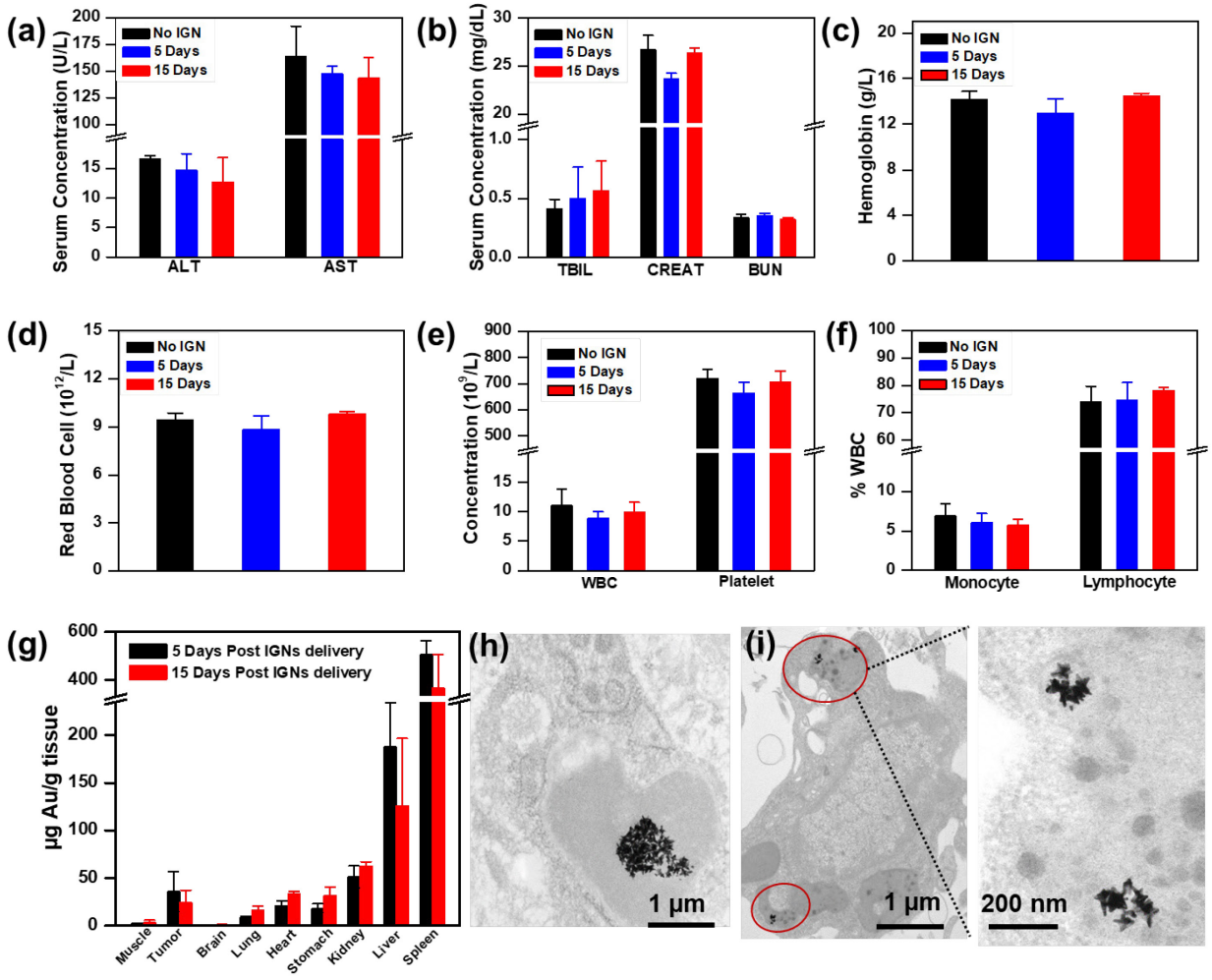

Figure 2. Toxicity and Biodistribution of IGNs. Serum inflammatory markers and complete blood count of tumor-bearing control mice without IGNs (n = 3) and mice that received intraperitoneal delivery of IGNs 5 days (n = 3) and 15 days (n = 3) post-delivery. Inflammatory markers including (a) liver enzyme, alanine aminotransferase (ALT) and aspartate aminotransferase, (AST), and (b) kidney markers, total bilirubin (TBIL), blood urea nitrogen, CREAT (creatinine), and blood urea nitrogen (BUN) showed no significant differences between control and IGN-injected mice. Complete blood analysis also showed no abnormalities in hematological parameters, including (c) hemoglobin, (d) red blood cells, (e) white blood cell (WBC) and platelet concentration, and (f) the white blood cell profile (% monocytes and % lymphocytes). (g) Biodistribution and clearance of IGNs confirmed with ICP-MS show Au in tumor, muscle, and major organs both 5 days (n = 3) and 15 days (n = 3) post IGNs delivery. TEM micrographs of IGNs in (h) Kupffer cells in liver and (i) intracellular vesicles in tumors.

Preclinical Evaluation and Biodistribution of IGNs. Prior to *in vivo* imaging, we performed an antibody-antigen binding assay similar to enzyme-linked immunosorbent assay (ELISA) to validate IGNs ability to specifically bind to CD8 and PD-L1 receptors (Figure S2). This *ex vivo*

study showed successful binding of IGNs to the respective antigen when conjugated with the corresponding mAbs. We evaluated the biocompatibility of IGNs *in vivo* at 5 and 15 days post intraperitoneal (IP) delivery of IGNs (0.06 mg IGNs/g mouse weight) to examine both near-term and longer-term impact. This dosage of IGNs is comparable or lower than other studies utilizing nanostars.[35, 36] We chose a murine model of melanoma for our study with Yale University Mouse Melanoma cell line variant 2.1 (YUMM 2.1) tumors that are highly immunogenic with intrinsically upregulated PD-L1 expression and high infiltration of $CD8^+$ T cells.[37] The toxicity of IGNs was studied by examining standard serum inflammatory markers to determine if IGNs elicit any immune response in mice. Alanine aminotransferase (ALT) and aspartate aminotransferase (AST) were used as indicators of liver function (Figure 2a), and total bilirubin (TBIL), creatinine (CREAT), and blood urea nitrogen (BUN) were used to measure renal function (Figure 2b).[38] Further, complete blood count (CBC) analysis, including hemoglobin, red blood cells, white blood cells, platelet concentration, monocyte counts, and lymphocyte counts (Figure 2c-f) was also examined in mouse serum. These serum markers were comparable to mice that received IGNs relative to control mice which received PBS. These observations were confirmed with hematoxylin and eosin (H&E) staining of major organs and tumors of mice that received IGNs, and no noticeable histopathological changes were observed (Figure S3). We note that the concentration of mAbs covalently bound to IGNs was <0.5 μg antibody/mouse (0.29 μg of anti-CD8 antibody/mouse and 0.22 μg of anti-PD-L1 antibody/mouse), which is a very low dose and should not contribute to any mAbs related toxicities (Figure S4). Quantitative ICP-MS analysis of Au in tumor and major organs that were retrieved 5 and 15 day post IP delivery of IGNs (Figure 2g) demonstrated IGNs were retained in tumors indicative of active targeting in TME as well as accumulation through the enhanced permeability and retention (EPR) effect. Table S3 shows the

concentration of IGNs in all organs. Only trace Au was found in brain tissue since the blood brain barrier prevents the entry of nanoparticles larger than 10 nm, and minimal Au was found in other organs. IGNs were predominantly cleared through the MPS organs, spleen and liver, *via* internalization by macrophages as expected for Au nanoparticles.[29, 39, 40] Transmission electron micrographs (TEM) confirm that IGNs were localized in Kupffer cells in the liver (Figure 2h), and in the tumor IGNs were observed in intracellular vesicles or lysosome-like structures (Figure 2i), suggesting internalization through receptor-mediated endocytosis.

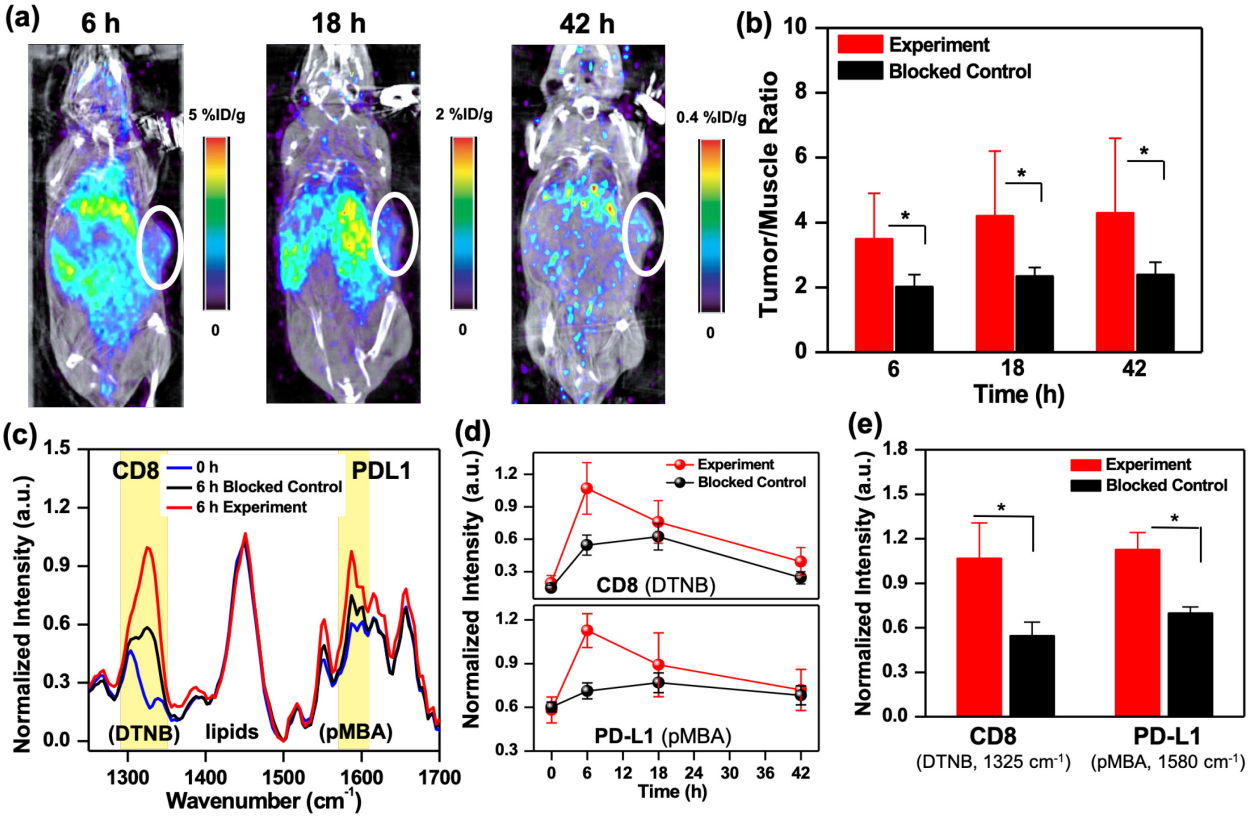

Figure 3. ImmunoPET-SERS Imaging with IGNs to Detect PD-L1 and CD8. (a) Whole body PET/CT images of mouse bearing YUMM 2.1 tumors at 6 h (1.02% ID/g), 18 h (0.48% ID/g) and 42 h (0.11% ID/g) post IGN delivery identifying tumor location by targeting both immunomarkers. (b) Longitudinal PET by examining tumor to muscle (T/M) ratio showing statistically significant differences in the uptake of IGNs in experimental tumors (n = 7) relative to blocked control (n = 5). (c) Normalized SERS spectra of tumors before IGNs delivery (0 h) and at maximum accumulation time (6 h) of experimental and blocked control mice. The dominant peak for Raman

tags DTNB (1325 cm^{-1}) and pMBA (1580 cm^{-1}) are highlighted in yellow. (d) Longitudinal SERS analysis where pMBA and DTNB peaks were normalized to the intrinsic lipid peak at 1440 cm^{-1}. (e) SERS quantification of PD-L1 and CD8 at maximum accumulation time indicating statistically significant differences (~49% difference in DTNB and ~38% in pMBA) between experiment (n = 4) and blocked control groups (n = 4). All ImmunoPET-SERS experiments were repeated 3 times. Here, * indicates $p \leq 0.05$.

Multimodal Multiplexed Immunoimaging. Each diagnostic technology has both merits and drawbacks, and a single technique cannot simultaneously achieve all of the desired characteristics of an ideal imaging modality. Recent efforts in immunoPET with radiolabeled mAbs have been very effective in tracking single immunomarkers *in vivo.*[41, 42] But multiplexing cannot be achieved with PET as signal between radionuclides cannot be distinguished. Without the ability to multiplex, patients would undergo multiple dosing of radiolabeled mAbs, repeated radiation exposure, and discomfort. Further, dynamic changes in immunomarkers during treatment would be missed as sequential dosing of different mAbs would require >1 week wait time between doses to allow for decay of the radiotracers. Here we show IGNs enable dynamic detection of both PD-$L1^+$ tumor cells and $CD8^+$ T cells *in vivo* by synergistically combining the advantages of immunoPET with SERS while overcoming limitations of each approach (Figure 3). Longitudinal immunoPET-SERS imaging was performed after IP delivery of 0.06 mg IGNs/g mouse weight at ~8MBq of radioactivity in YUMM 2.1 tumor-bearing mice. The longer plasma half-time of IGNs relative to radiolabeled mAbs enabled extended longitudinal study of the two immunomarkers in the TME. First, PET and computed tomography (CT) images were acquired in mice post IGNs administration *via* whole body scans, which provided a depth-resolved view of the localization of IGNs in tumors with high sensitivity. The decrease in signal in PET images (Figure 3a) was reflective of the rapid decay of ^{64}Cu (half-life ~12 h), and such a trend has been observed previously for chelated ^{64}Cu conjugates.[43, 44] To account for the decay of ^{64}Cu, the ratio of tumor

to adjacent muscle (T/M) is obtained. T/M ratio has been shown in both mouse models and in patients as a more accurate measure of tracer uptake than absolute values in tumor.[45, 46] The specificity of IGNs in immunomarker detection was demonstrated with pre-blocked control mice, where both PD-L1 and CD8 were pre-blocked by administering a saturating dose of anti-PD-L1 and anti-CD8 mAbs (200 μg each). Longitudinal PET images of pre-blocked control mice showed lower signal in tumors (Figure S5), a trend supported by other PET imaging studies.[47, 48] Quantitative PET analysis of the T/M ratio showed high signal in tumors of experimental mice and statistically significant differences (SSD) relative to blocked control mice (Figure 3b). Note that the signal in liver and spleen is not entirely resulting from the use of nanoparticles, as the utility of ^{64}Cu tracers has also shown high background activity in the liver of patients.[49] We also observed minimal difference in PET analysis of liver/muscle, kidney/muscle, and spleen/muscle ratios (Figure S6) between experimental and control mice, indicating that IGN biodistribution was similar in both groups, and SSD were only observed in tumors.

Immediately following PET, multiplexed detection with SERS was achieved with two different Raman labels which delineated PD-L1 and CD8 in the tumor with high spatiotemporal resolution. SERS measurements were acquired using a custom portable Raman setup equipped with a 785 nm continuous-wave laser at 80 mW power and a fiber optic probe. SERS spectra were acquired through the skin by placing the probe at different locations on the tumor; spectra were then averaged, smoothed using a Savitzky-Golay filter,[50] and background subtracted. The SERS peaks indicating the detection of $CD8^+$ T cells (DTNB, 1325 cm^{-1}) and $PD\text{-}L1^+$ cells (pMBA, 1580 cm^{-1}) in the tumor were normalized to the 1440 cm^{-1} peak corresponding to lipids and proteins,[51] which remained consistent within the same mouse during time-course study. Individual spectra acquired at different locations on the tumor of mice in both experimental and control groups did

not show significant intra-mouse variability (Figure S7). The averaged SERS spectra of different mice (Figure 3c) before IGN delivery (0 h) and six hours post-delivery (6 h) showed that IGNs accumulated in tumors enabling highly specific multiplexed detection distinguishing both PD-L1 and CD8 in experimental tumors relative to the blocked control. It is noteworthy that labeling the mAbs directly with the Raman tags (without the nanoparticles) would not have enabled any meaningful *in vivo* signal as Raman scattering is intrinsically very weak and often overwhelmed by the fluorescence background of biological tissue. As shown in our previous work, the gold nanostars amplify the Raman signal by $10^9 – 10^{12}$, where the signal is higher at the protrusion tips necessary for highly sensitive signal to noise *in viv*o.[19] Longitudinal SERS (Figure 3d) showed maximum accumulation of IGNs occurred at 6 h post-delivery and a decrease in SERS intensity at 42 h. Observed SERS intensity trend was attributed to the surface-weighted characteristics of SERS typical for most optical techniques, where signal is higher near the measurement surface (here mouse skin) closest to the Raman laser probe. Therefore, IGNs accumulating near the tumor surface were preferentially visualized in earlier time-points. As IGNs transported from the peripheral vasculature and distributed within the tumor core at later time points, the SERS intensity decreased at 42 h. This trend follows literature evidence that nanoparticles enter solid tumors through leaky vasculatures *via* the EPR effect and concentrate near the peripheral vasculature rich in blood vessels. In the case of well-vascularized tumors (such as YUMM 2.1), in >24 h nanoparticles may transport into the tumor core *via* various pathways, such as intercellular or transcellular transport, or remain in the outer tumor layer in the case of necrotic or poorly vascularized solid tumors.[52] TEM images taken from areas of the tumor core showed IGNs do transport beyond the periphery in the YUMM 2.1 model (Figure 2i). PET provided a depth-resolved field of view of IGNs distribution in tumors even at 42 h. The specificity of our approach

was demonstrated by revealing SSD between experimental and control mice. Quantitative SERS at 6 h indicated SSD and lower signal in CD8 (49% lower DTNB signal) and PD-L1 (38% lower pMBA signal) in the blocked control mice relative to experimental mice (Figure 3e). *In vivo* endpoints with immunoPET-SERS were validated by flow cytometry analysis of excised tumors (Figure S8). Flow results showed robust blocking of both immunomarkers and a decrease in PD-L1$^+$ tumor cells (42.6% to 0.34%) and CD8$^+$ cells (7.47% to 0.086%) in the blocked control.

IGNs Monitor Response to Immunotherapies. In addition to multiplexed detection of immunomarkers, we also demonstrated the utility of IGNs to monitor response to immunotherapies and distinguish responders from those nonresponsive to treatment. Unlike chemotherapy and radiation, accurate response to treatment is imperative in immunotherapies as patients show distinct radiologic response patterns, including pseudoprogression[53], that are not adequately captured by the traditional Response Evaluation Criteria in Solid Tumors (RECIST).[54] Therefore, dynamic imaging of both PD-L1$^+$ tumor cells and CD8$^+$ T cells is vital to accurately reflect the changes in immunomarker localization during the course of treatment since both of these cell types modulate the immune TME. Here, we delivered checkpoint blockade therapy to both BRAF-mutant YUMM 2.1 and NRAS-mutant YUMM 10.1 melanoma tumors treated with combinatorial PD-L1 and CD137 agonists. BRAF mutations are most prevalent in melanoma and responsive to immunotherapies,[55] whereas NRAS mutations are most aggressive and nonresponsive to checkpoint blockade.[56] It has been previously shown that co-stimulation with CD137 results in expansion of effector T cells, production of cytokines, and resistance to suppression by regulatory T cells,[21, 22] and has demonstrated synergistic antitumor effects when combined with anti-PD-L1 mAbs in clinical trials (NCT02451982, NCT03414658).

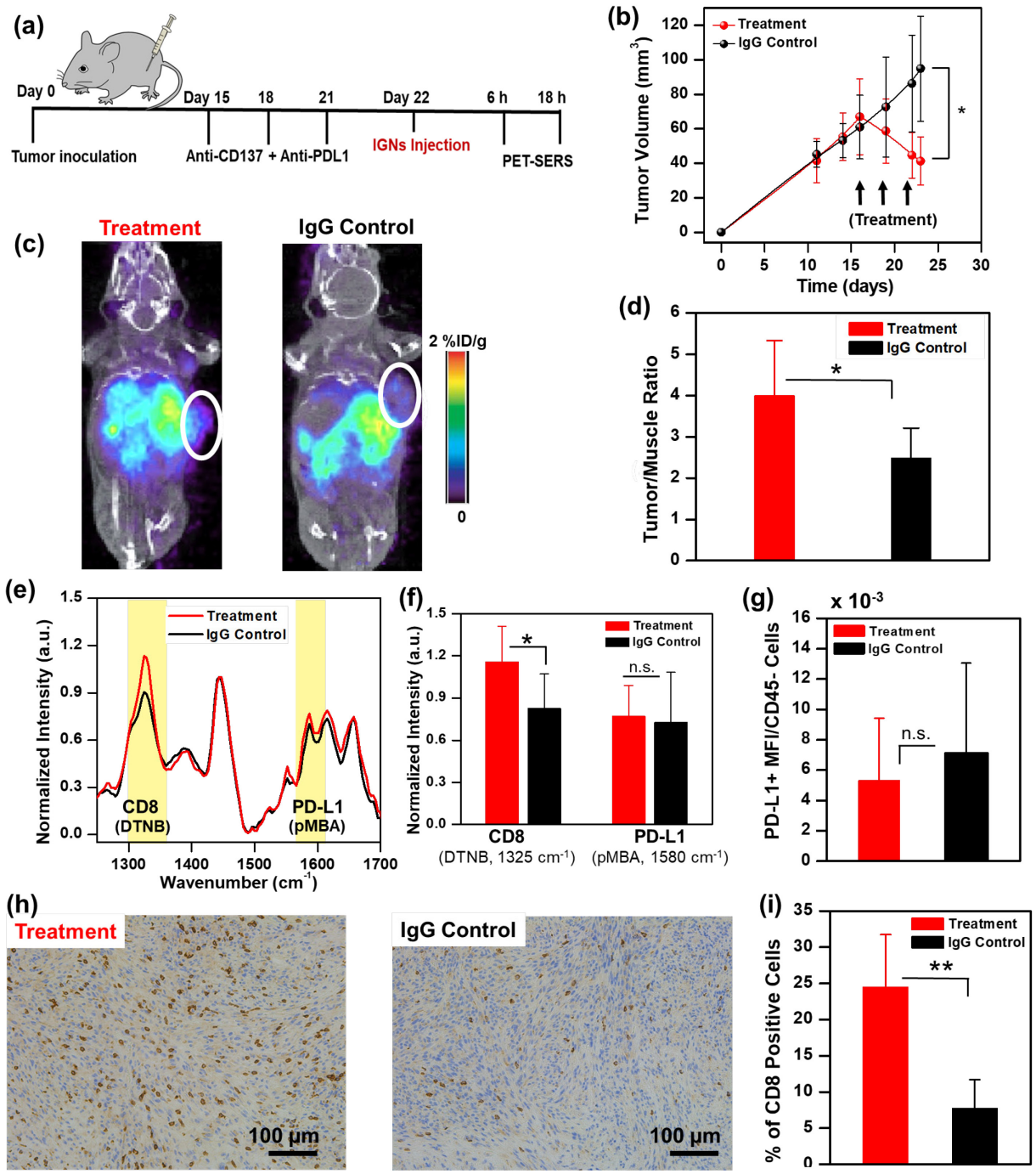

Figure 4. ImmunoPET-SERS Imaging to Monitor Immunotherapy Response. (a) Mice bearing YUMM 2.1 tumors were treated with 3 doses of combinatorial immunotherapy of anti-CD137 + anti-PD-L1 followed by IGNs delivery and imaging 24 h after the last treatment. Control mice received isotype-matched immunoglobulin G (IgG) treatment (n = 5 for both groups). (b) Tumor volumes decreased with immunotherapy. (c) PET-CT images of mouse revealed a higher localization of IGNs in tumors of treatment group (0.58% ID/g) relative to IgG control (0.31 % ID/g). (d) Corresponding PET quantification showing statistically significant differences in tumor/muscle ratio between treatment and control groups. (e) Averaged SERS spectra of treatment and IgG control group. (f) Corresponding SERS quantification showing a statistically significant

increase in $CD8^+$ signal. (g) Flow cytometry showed minimal change in PD-L1 status after immunotherapy. (h) Immunohistochemistry images and (i) IHC DAB stain quantification of % $CD8^+$ cells confirmed significantly higher $CD8^+$ tumor infiltrating lymphocytes in mice treated with immunotherapies (n = 5) relative to control group (n = 5). Here, * indicates $p \leq 0.05$, ** indicates $p \leq 0.01$, and n.s. indicates not significant. All *in vivo* and *ex vivo* experiments were repeated 3 times.

First, YUMM 2.1 tumor-bearing mice were treated with 3 doses of combined anti-PD-L1 (200 μg/mouse) and anti-CD137 (110 μg/mouse) therapeutic antibodies. IGNs were delivered 24 h after the last treatment followed by ImmunoPET-SERS to monitor dynamic changes in CD8 and PD-L1 status (Figure 4a) post-treatment. Mouse weight did not decrease over the course of therapy, demonstrating minimal adverse effects (Figure S9). Mice with a tumor volume decrease of >20% from baseline to 22 d post-treatment were defined as responders and all others were categorized as nonresponders. A decrease in tumor volume (Figure 4b) indicated that YUMM 2.1 tumors responded to combinatorial immunotherapy relative to control mice that received isotype-matched anti-IgG (310 μg/mouse). PET-CT images showed that IGNs accumulated in both tumors and major organs of mice supporting our biodistribution studies (Figure 4c). Quantitative PET signal analysis of T/M ratios indicated an increase in PET signal for the experimental group relative to control group, and SSD between treatment and control mice (Figure 4d). To delineate if the observed increases in PET intensities corresponded to changes in PD-L1, or infiltration of $CD8^+$ T cells, or both, multiplexed SERS analysis was performed. SERS showed (Figure 4e) proliferation of $CD8^+$ T cells in tumors of the treated mice (indicated by 1325 cm^{-1} DTNB peak), which corresponded well with PET results and the decrease in tumor volume in the treatment group. Success in immunotherapies in the tumor milieu is followed by recruitment and infiltration of activated $CD8^+$ T cells in the TME. Increase in $CD8^+$ cells gave rise to higher accumulation of IGNs/anti-CD8/DTNB/^{64}Cu in the tumor post-treatment. Thus, multimodal imaging of the tumors

showed an increase in T/M in PET and higher DTNB signal in SERS in the treatment group, relative to the IgG control group. SERS spectral analysis of PD-L1 (indicated by 1580 cm^{-1} pMBA peak) showed minimal differences between treated and control mice (Figure 4f). This is not surprising as YUMM 2.1 cells have a constitutionally high expression of PD-L1, and thus an upregulation of PD-L1 resulting from interferon gamma (IFN-γ) was not significant. Flow cytometry analysis of YUMM tumors showing the expression level of PD-L1 receptors (in CD45 negative subset cells) verified our SERS results (Figure 4g). *In vivo* imaging results were validated with IHC of excised tumors (Figure 4h) and spleen (Figure S10a,b) stained for $CD8^+$ T cells. IHC images, and quantification of number of 3,3'-diaminobenzidine (DAB) stained $CD8^+$ cells (Figure 4i) confirmed expansion of activated $CD8^+$ tumor infiltrating lymphocytes (TILs) in mice treated with immunotherapies (23.7 ± 5.3% positive $CD8^+$ cell) relative to the IgG control (7.6 ± 5.3%). We also quantified the intensity of DAB for the $CD8^+$ stain (Figure S11a) and observed similar trends for treated (1.77 ± 0.73%) and control mice (0.42 ± 0.18%). Localization of $CD8^+$ T cells in the splenic T cell zones (Figure S10a) also suggested systemic T cell activation and expansion in the peripheral organ. H&E staining of tumor sections confirmed that immunotherapies did not alter tissue histomorphology in both treatment and control groups (Figure S12a,b).

We further demonstrated the efficacy of IGNs in distinguishing responders from those nonresponsive to immunotherapies by examining NRAS mutant YUMM 10.1 murine melanoma tumors. YUMM 10.1 tumors were treated with a similar combinatorial immunotherapy regimen, and antiIgG mAbs in control mice. YUMM 10.1 tumors were nonresponsive to combination anti-PD-L1 and anti-CD137 treatment as observed in tumor volume measurement (Figure 5a). ImmunoPET-SERS imaging 24 h post-IGN delivery supported this trend where whole-body PET-CT scans showed minimal differences in PET signal between treatment and control groups (Figure

5b), verified with PET quantification of T/M ratio (Figure 5c). SERS measurement of tumors delineated both $CD8^+$ (DTNB at 1325 cm^{-1}) and PD-L1 (pMBA at 1580 cm^{-1}) signals and showed minimal differences between experimental and control mice (Figure 5d,e). *In vivo* endpoints were validated with flow cytometry analysis of PD-$L1^+$ cells in CD45- subset cells (Figure 5f) and immunohistochemistry of $CD8^+$ cells (Figure 5g,h), which supported our findings with ImmunoPET-SERS showing minimal difference in the two immunomarkers between treatment and control mice. We note that YUMM 10.1 is an immunogenic tumor model with constitutively high $CD8^+$ T cells infiltration even without immunotherapy as evidenced by IHC of control tumors (Figure 5h). Additional histopathology findings of YUMM 10.1 tumors treated with immunotherapies are provided in Figure S10c,d and Figure S12c,d.

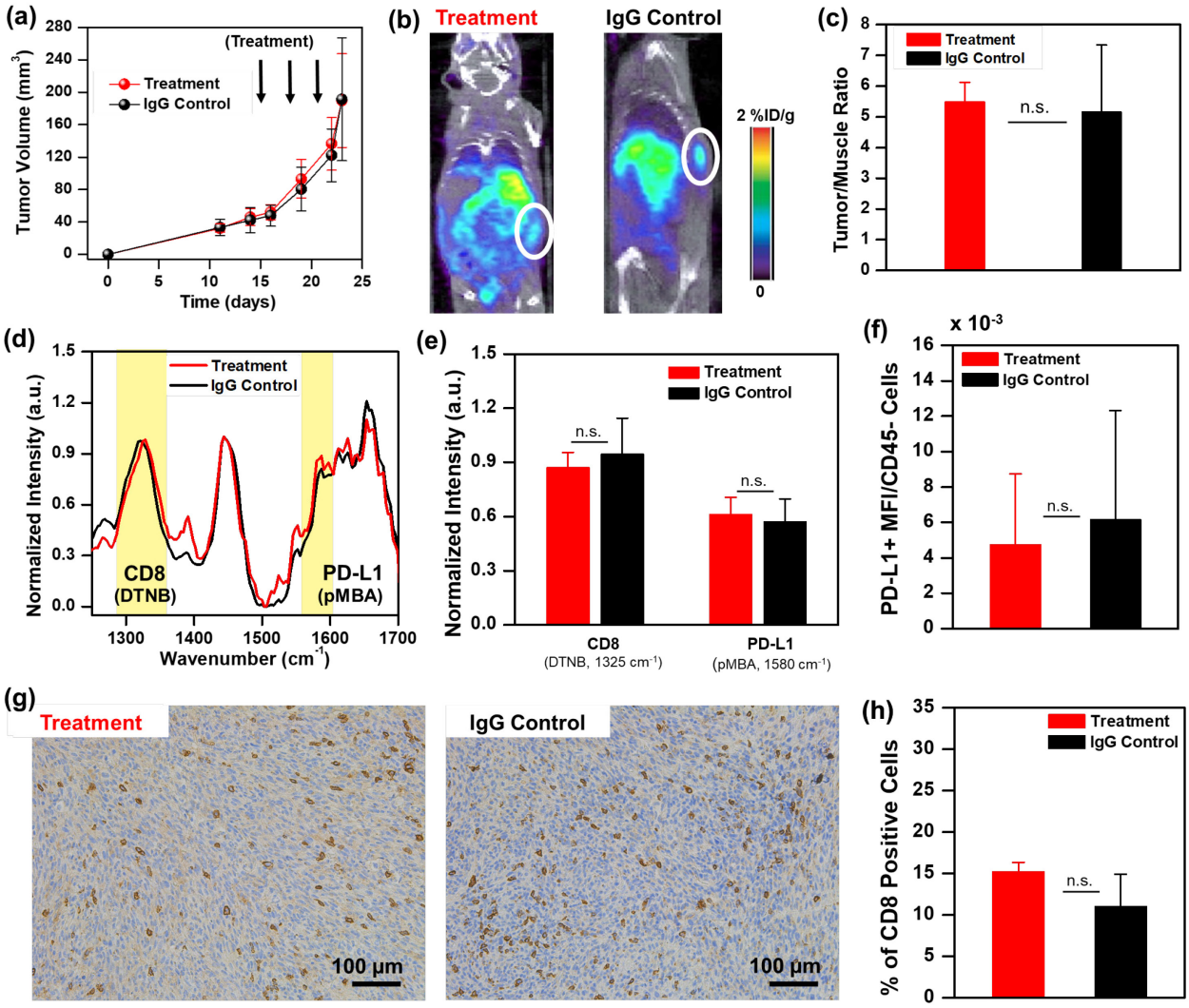

Figure 5. ImmunoPET-SERS Imaging to Distinguish Nonresponders. Mice bearing NRAS mutant YUMM 10.1 melanoma tumors were treated with 3 doses of combinatorial immunotherapy of anti-CD137 + anti-PD-L1 followed by IGN delivery and imaging 24 h after the last treatment. Control mice received isotype-matched IgG treatment. (a) Tumor volumes did not decrease for mice receiving immunotherapy (n = 7) relative to IgG control (n = 7). (b) PET images of mouse revealed similar localization of IGNs in tumors of treatment group (0.64% ID/g) relative to IgG control (0.7 % ID/g). (c) Corresponding quantitative PET analysis showing tumor/muscle ratio. (d) Averaged SERS spectra shown for immunotherapy and control group. (e) Corresponding SERS quantification showed no difference in both CD8 and PD-L1 signals (n = 5 for both groups). (f) Flow cytometry showed minimal change in PD-L1 status in both groups (n = 5 for both groups). All ImmunoPET-SERS experiments were repeated 2 times. (g) Immunohistochemistry of tumors shows $CD8^+$ TILs in both treatment and control groups. (h) IHC DAB quantification of % $CD8^+$ cells showed no difference in cell counts between both groups. The differences were statistically not significant (n.s.) for (a), (c), (e), and (h).

CONCLUSIONS

In summary, we demonstrated the design and *in vivo* validation of an innovative and clinically-translatable nanoprobe, IGNs, for real-time immunological tumor profiling of multiple immunomarkers engaged in the immune TME. Our results demonstrated that ImmunoPET-SERS imaging with IGNs facilitated both biomarker screening before treatment to identify targetable pathways, and accurately monitored response to immunotherapies to improve the clinical outcome of PD-1/PD-L1 blockade. The results of this work will ultimately allow translation of IGNs from preclinical mouse models to clinically relevant systems. PET is already in clinic, gold nanoparticles are in the clinical trials,[57] and SERS is facilitated by NIR light that has a 2 – 4 cm penetration depth,[32, 33, 58] enabling its utility in multiple organs including breast,[59] brain,[60] and liver[61] useful for both localized and metastatic disease. FDA-approved optical fibers can also now deliver light in deep tissues[62, 63] allowing clinical translation of SERS in various tumor types beyond melanoma. Early detection of immunomarkers will improve therapeutic outcome for responders and accelerate clinical decisions for those requiring alternative treatment as well as minimize toxicities and high costs of unsuccessful therapies for nonresponders. Further, our platform can be expanded beyond melanoma to a multitude of malignancies by targeting other inhibitory ligands (TIM3, LAG3, PSGL-1) and other immune cell populations ($CD4^+$ T cells, NK cells). Moreover, whereas this proof of concept study enabled us to track two immunomarkers with multiplexed SERS, future work will expand the utility of IGNs to detect ~10 biomarkers[64, 65] for screening heterogeneous tumors and monitoring treatment response.

MATERIALS AND METHODS

Synthesis of Gold Nanostars (IGNs). IGNs were synthesized with a biological buffer, (4-(2-hydroxyethyl)-1-piperazineethanesulfonic acid) (HEPES) through a one-step and seedless mediated method that was previously described by our group. Briefly, 18 mL of ultrapure water at 18 MΩ was added to 12 mL of 270 mM HEPES buffer at pH 7.40 ± 0.2. Next, 300 µL of 20 mM chloroauric acid was added. The solution was then mixed by gentle inversion and reacted for 75 min at room temperature. Both IGNs synthesis materials, gold(III) chloride trihydrate ($HAuCl_4$), and HEPES were purchased from Sigma-Aldrich.

Functionalization of IGNs. Raman tags, 4-mercaptobenzoic acid (pMBA) and 5,5'-Dithiobis(2-nitrobenzoic acid) (DTNB), were purchased from TCI America. Bifunctional linker, orthopyridyl-disulfide poly(ethylene glycol)-N-hydroxysuccinimide ester (OPSS-PEG-NHS ester, M_w 2000), was purchased from JenKem Technology. To conjugate Raman tags to the IGNs surface, 6 µL of 10 mM pMBA or DTNB (in 100% ethanol) were added to 60 mL of IGNs and reacted for 15 min at 4 °C. To remove excess Raman tags, the IGNs was centrifuged at 6000 rpm for 10 min. To functionalize targeting antibodies to IGNs, OPSS-PEG-NHS ester linkers were first reacted with anti-PD-L1 (Bio X Cell BE0101, clone 10F.9G2) and anti-CD8 (Bio X Cell BE0004-1, clone 53-6.7) antibody. Briefly, 8 µL of 80 mg/mL OPSS-PEG-NHS was added to 72 µL of 1 mg/mL antibody and allowed to react in 100 mM (pH 8.4 ± 0.1) sodium bicarbonate ($NaHCO_3$) buffer at 4 °C for 24 h. After, 80 µL of OPSS-PEG-anti-CD8 or OPSS-PEG-anti-PD-L1 was added to 6 mL of Raman-labeled-IGNs at 1.14 mg/mL. The IGNs solution was then mixed on an inverter for another 24 h. Next, to conjugate the chelator, 1,4,7,10-Tetraazacyclododecane-1,4,7,10-tetraacetic acid (DOTA) to gold, OPSS-PEG-NHS ester linkers were reacted with 1.4 mg of DOTA-amine (Macrocyclics) at 1:1 ratio for 10 h. OPSS-PEG-DOTA was then reacted with

IGNs for 12 h. Lastly, the fully functionalized IGNs (IGNs/anti-CD8/DTNB or IGNs/anti-PD-L1/pMBA) were centrifuged at 4000 rpm for 10 min twice and resuspended at a concentration of 5 mg/mL.

Characterization of Functionalized IGNs. The plasmon resonance of 1.5:1 mixture of anti-PD-L1-pMBA-IGNs and anti-CD8-DTNB-IGNs was measured with a Varian Cary 5000 UV-Vis NIR spectrophotometer. The size and shape of IGNs were visualized with an Osiris transmission electron microscope (TEM) at 200 keV. The Raman spectra of IGNs mixture at 1.5:1 (IGNs/anti-PD-L1/pMBA and IGNs/anti-CD8/DTNB) was obtained with a custom Raman setup with a 785 nm laser at 80 nW. A Malvern Nano ZS dynamic light scattering apparatus was used to measure both the hydrodynamic size and the zeta potential of IGNs before and after functionalization.

ELISA Binding Assays and Antibody Quantification. ELISA binding assay of IGNs/anti-CD8/DTNB was performed with a mouse CD8 alpha ELISA kit (Abcam, ab238263), and that for IGNs/anti-PD-L1/pMBA was performed with a mouse PD-L1 DuoSet ELISA kit (R&D Systems, DY1019-05). All ELISA sandwich assays were performed according to the manufacturer provided procedure, but detection antibodies were replaced with either IGNs/anti-CD8/DTNB or IGNs/anti-PD-L1/pMBA. ELISA quantification of anti-CD8 or anti-PD-L1 antibodies on IGNs was performed by using secondary antibody (ThermoFisher, 31470) conjugated with horseradish peroxidase and 3,3′,5,5′-Tetramethylbenzidine (TMB) substrate. Briefly, IGNs/anti-PD-L1/pMBA or IGNs/anti-CD8/DTNB was blocked with bovine serum albumin (BSA) in phosphate buffered saline for 1 h then subsequently incubated with secondary antibody at 0.1 mg/mL for 1 h at room temperature. The sandwich complex was centrifuged and washed with washing buffer three times to remove excess free secondary antibody. TMB solution

was then incubated with the sandwich complex for 15 min. The reaction was quenched with 2 N sulfuric acid. Colorimetric readings were performed at 450 nm.

YUMM 2.1 Xenograft Model and *In Vivo* Multimodal Multiplexed Imaging. Murine melanoma cell lines YUMM2.1 and YUMM10.1, generated by Dr. Marcus Bosenberg (Yale University), were provided by Ann Richmond Lab (Vanderbilt University School of Medicine) with permission from Dr. Richmond and were cultured in Dulbecco's Modified Eagle's medium (DMEM, Gibco), supplemented with 10% fetal bovine serum (FBS, Sigma Aldrich), 1% penicillin streptomycin (Gibco), and 1x MEM non-essential amino acid (Sigma Aldrich). YUMM 2.1 cells were cultured at 37 °C and 5% CO_2. To develop xenografts in B6 (C57BL/6J, Jackson laboratory) mice, 1.5 million YUMM 2.1 cells per 100 µL were injected into the right flank of each mouse. The xenografts were monitored with a caliper every two days. Once the tumor reached 5 mm in diameter, functionalized IGNs, IGNs/anti-PD-L1/pMBA and IGNs/anti-CD8/DTNB at a 1.5:1 ratio were administered IP into mice for PET and SERS imaging experiments. Each mouse was injected with 1.2 mg of IGNs with 800 µCi of ^{64}Cu activity. For blocked control, 200 µg anti-PD-L1 (Bio X Cell, clone 10F.9G2) and 200 µg of anti-CD8 (Bio X Cell, clone 53-6.7) antibodies were injected (IP) concurrently with IGNs at the other side of abdominal cavity. Note, the antibodies utilized for pre-blocked control were the same clone as the antibodies used to functionalize IGNs.

Mice bearing YUMM 2.1 xenograft (for both experiment and pre-blocked control groups) were first placed in a small animal imaging PET/CT machine (Inveon microPET/CT from Siemens Preclinical, Knoxville TN). Mice were imaged at 6, 18, and 42 h post IGNs administration. The mice were imaged in an Inveon microPET/CT (Siemens Preclinical, Knoxville TN) while under 2% isoflurane anesthesia. All PET data sets were reconstructed using the MAP algorithm into 128

× 128 × 95 slices with a voxel size of 0.095 × 0.095 × 0.08 cm^3 at a beta value of 0.01. The PET and CT images were uploaded in the medical imaging tool Amide (www.sourceforge.amide.com). The PET images were normalized to the injected dose. Regions-of-interest (ROIs) were drawn around the tumor, spleen, liver, kidneys, and muscle (hind limb) for reference. The mean radiotracer concentrations within these ROIs were measured in units of percent injected dose per unit volume (%ID/g).

Once the tumor xenografts were identified with PET, SERS imaging was then performed at the same time points as PET imaging (6, 18, and 42 h post IGNs administration) at eight different sites of the tumor xenograft with a custom portable Raman spectroscopy system. Measurements were taken for 10 s with a 785 nm diode laser (Innovative Photonics Solutions, Monmouth Junction, NJ) that delivered 80 mW of power using a custom-made fiber optic probe (EmVision, Loxahatchee, FL), which was gently placed on the xenograft. Wavelength calibration of the Raman system was performed using a neon-argon lamp, while acetaminophen and naphthalene standards were used to determine the exact excitation wavelength for calculating Raman shifts. Raman scattering from the samples was first collected from the fiber optic probe, and then by an imaging spectrograph (Holospec f/1.8i, Kaiser Optical Systems, Ann Arbor, MI) coupled to a thermoelectrically cooled CCD camera (PIXIS: 256BR, Princeton Instruments, Princeton, NJ).

The Raman system was corrected for spectral response using a National Institute of Standards and Technology (NIST) calibrated tungsten lamp. Spectra were smoothed with a Savitzky-Golay filter, background subtracted, and fluorescence subtracted using a modified polynomial fit method as previously described. At each time point, both DTNB (1325 cm^{-1}) and pMBA (1580 cm^{-1}) peaks were normalized to 1440 cm^{-1} biological peak (corresponding to CH_2 stretching), which did not change over time.

***In Vivo* Multimodal Multiplexed Imaging to Monitor Treatment Response.** 1.5 million YUMM 2.1 cells per 100 μL were injected into the right flank of each mouse to develop tumor xenografts. Once the tumor reached 5 mm in diameter, immunotherapy treatment or IgG control injection commenced. Each treatment mouse received 3 doses of 115 μg of anti-CD137 antibodies (Bio X Cell BE0239, clone 3H3) and 200 μg of anti-PD-L1 (Bio X cell BE0101, clone 10F.9G2) antibodies every 3 days. Each IgG control mouse received 3 doses of 115 μg of IgG2a isotope control (Bio X Cell, BE0089) and 200 μg of IgG2b isotope control (Bio X cell, BE0090) every 3 days. Tumor sizes were measured with a caliper every 2 days. Mice weight was also monitored to ensure the therapy did not cause any extraneous side effects. A day after the last treatment, mice were administrated with functionalized IGNs, IGNs/anti-PD-L1/pMBA and IGNs/anti-CD8/DTNB at 1.5:1 ratio for PET/SERS imaging. PET imaging and Raman measurement were performed in the same manner as previously described.

Toxicity Study of IGNs *In Vivo*. 1.5 million YUMM 2.1 cells per 100 μL were injected into the right flank of each mouse to develop tumor xenografts. Once tumors reached 5 mm in diameter, functionalized IGNs, IGNs/anti-PD-L1/pMBA and IGNs/anti-CD8/DTNB at 1.5:1 ratio were administered IP into mice. Mice were sacrificed either 5 or 15 day post particle injection. Cardiac puncture was performed as soon as the mice were euthanized to obtain 500 μL of blood per mouse for both complete blood count (CBC) and serum liver/kidney metabolite studies. In addition, tumor, heart, liver, kidney and spleen of each mouse were retrieved and fixed in 6% formalin for hematoxylin and eosin (H&E) staining. The toxicity study was performed at Vanderbilt University Medical Center – Translational Pathology Shared Resources. Complete blood counts were performed in the Forcyte Veterinary Hematology Analyzer manufactured by

Oxford Science. Blood chemistries were performed on the Vet Axcel Chemistry Analyzer manufactured by Alfa Wassermann.

Inductively Coupled Plasma-Mass Spectrometry (ICP-MS). Mice bearing YUMM 2.1 xenograft were injected with functionalized IGNs, anti-PD-L1-pMBA-IGNs and anti-CD8-DTNB-IGNs at 1.5:1 ratio. For each mouse, the tumor, stomach, liver, spleen, kidneys, heart, lungs, brain and muscle were retrieved either 5 or 15 days post particle injection. After dissection, the tissues were frozen immediately in liquid nitrogen. A lyophilizer was first used to remove any water in the tissues. Next, dried tissues were then place in 75 vol. % trace metal grade aqua regia (HCl from Fisher Scientific, A508-P500 and HNO_3 from Fisher Scientific, A509-P500) for 72 h. Aqua regia was then boiled off and the tissue samples were then redissolved in 10 mL of 2 vol. % aqua regia. Filters (0.4 μm) were used to remove any impurities prior to ICP-MS readings.

ICP-MS measurement and analysis were performed at Vanderbilt University, Department of Civil and Environmental Engineering. Perkin Elmer model ELAN DRC II was operated in standard mode for all readings. The setting of the instrument was 1.5 kW radio frequency power, 15 L/min argon plasma flow, 1 L/min nebulizer flow, and 1 s integration time for 3 replicates. Six-point calibration curve was performed for gold isotope 197 between 0.05 μg/L and 500 μg/L. Analytical blanks and check standards (0.5 μg/L) were measured for every 3 – 5 samples to ensure the readings were within 15% of the specified value.

Transmission Electron Microscope Imaging of Tissues. Mice bearing YUMM 2.1 tumor xenograft were injected with functionalized IGNs, IGNs/anti-PD-L1/pMBA and IGNs/anti-CD8/DTNB at 1.5:1 ratio. The mice were sacrificed at 6 h post particle administration, and the tumor xenograft, liver, and spleen were retrieved. All samples were sectioned into 1 mm by 1 mm pieces with razor blades and fixed in 2.5% gluteraldehyde in 0.1M cacodylate buffer (pH 7.4 ± 0.1)

first at room temperature for 1 h and then 24 h at 4 °C. The specimens were further processed for transition electron microscopy imaging by the Vanderbilt Cell Imaging Shared Resource facility. The tissue samples were further fixed with 1% osmium tetraoxide and washed with 0.1 M cacodylate buffer. Sample dehydration was done serially with graded ethanol. Three 100% ethanol exchanges and two exchanges of pure propylene oxide (PO) were performed. The samples were then filtrated with 25% Epon 812 resin and 75% PO for 30 min at room temperature, then with 50% Epon 812 resin for 1 h, and 50% PO overnight. Subsequently, all samples went through a Epon 812 resin and PO (3:1) exchange and incubated with pure epoxy resin overnight. Before sample embedding, two exchanges of pure epoxy resin were performed. Lastly, polymerization was done at 60 °C for 48 h. Once the embedding process was complete, the samples were first sectioned at 500 – 1000 nm, and then were cut for 70 – 80 nm ultra-thin sections. The samples were placed on copper grids and stained with uranyl acetate (2%) and Reynold's lead citrate. TEM imaging was performed with the Philips/FEI Tecnai T12 electron microscope.

Quantification of CD8 Immunohistochemistry. Images were captured with a Leica SCN400 Slide Scanner automated digital image system from Leica Microsystems with 20X magnification to a resolution of 0.5 μm/pixel. Cell identification were performed either with a standard Ariol analysis scripts (% cell) or by FIJI[66] (ImageJ-based open-source software, % intensity). For Ariol analysis scripts, both brown (DAB) positive cells and blue (Hematoxylin only) negative cells were distinguished by setting upper and lower thresholds for color, saturation, intensity, size, roundness, and axis length. For the FIJI algorithm, color deconvolution was used to extract and threshold positively stained areas. Resulting binary images were then used to calculate integrated density values.

Flow Cytometry Analysis. YUMM 2.1 and YUMM 10.1 tumors were developed as previously described. Tumors were treated with blocking antibodies, anti-PD-L1 and anti-CD137 combination treatment, or IgG treatment. Harvested tumors were mechanically dissociated with an OctoMACS separator and digested in a solution of 125 μg/mL−1 Deoxyribonuclease I (Worthington) and 500 μg/mL−1 Collagenase III (Worthington) in RPMI media for 60 min at 37 °C. Tumors were then strained through a 40 μm cell strainer and further treated with ACK Lysing Buffer (Gibco). Cell suspensions (100 μL) for each sample were transferred into a 96-well plate and treated with FcX. Samples were stained with antibodies PE-PD-L1, B7-H1 (BioLegend 124307, clone 10F.9G2), FITC- CD8a (ThermoFisher Scientific 11-0081-82, clone 53-6.7), and APC/Cy7 - CD45 (Biolegend 103115, clone 30-F11). PE, phycoerythrin; APC, allophycocyanin; Cy, cyanine; FITC, Fluorescein isothiocyanate. After staining, cells were washed with PBS twice, and then suspended in PBS containing 2% FBS and 200 nM 4′,6-diamidino-2-phenylindole before analysis. Flow cytometry analysis was performed on a BD LSR Fortessa or BD LSR II flow cytometer.

Statistical Analysis. All data are presented as mean ± standard deviation. The sample sizes were estimated based on our previously published work on SERS *in vivo*.[20] Whereas that work was performed in immunocompromised nude mice, it directed us to the number of mice that should be used for good signal to noise ratio *in vivo*. Power analysis was performed and power level was set to 80% and confidence level was set to 95%. Differences between groups were assessed using Excel with paired or unpaired two-sided Student's t-tests for the calculation of P values. Here, * indicates $p \leq 0.08$, ** indicates $p \leq 0.05$, and *** indicates $p \leq 0.01$.

ASSOCIATED CONTENT

Supporting Information

The Supporting Information is available free of charge on the ACS Publication website at DOI:

Additional schematic for mAbs and DOTA conjugation to IGNs, IGNs stability and shelf life studies, IGNs antibody binding assays, quantitative ICP-MS analysis of biodistribution of IGNs, histopathology of tumor and major organs for IGNs toxicity study, ELISA quantification of IGNs antibodies, longitudinal PET images of blocked control mouse, quantification of PET signals in major orangs, examples of individual SERS spectrum, flow cytometry of YUMM 2.1 cell line targeting CD8 and PD-L1, body weight of mice bearing YUMM 2.1 xenograft treated with or without immunotherapy, quantification of tumor CD8 IHC by intensity, and CD8 IHC and histopathology of spleen and tumor of mice treated with or without therapy

AUTHOR INFORMATION

Corresponding Author

*E-mail: rbardhan@iastate.edu

Author Contributions

YO and RB conceived the idea, directed the project, and wrote the manuscript. YO and JAW designed the IGNs and determined the detailed chemistry. YO and XW performed the majority of the IGN synthesis and animal experiments. CJ, AV, and JB provided the melanoma cell lines, edited the manuscript and intellectually contributed in the discussions corresponding to immunotherapies and immunoimaging. DS and JTW assisted with flow cytometry measurements

and analysis. ODA and AM-J built the custom portable Raman spectroscopy instrument and helped with fluorescent subtraction of *in vivo* SERS data. ECL helped with further *in vivo* SERS data analysis. RCD contributed in biodistribution study and ICPMS measurements. KLB provided pathological insights on IHC and H&E staining of tissues our studies. MT performed PET measurements and analysis. MR and AR assisted with IHC analysis, quantification, and interpretation of the results.

Conflict of Interests

The authors declare that they have no competing interests.

ACKNOWLEDGMENTS

We acknowledge Jennifer Bateman for her assistance with the portable Raman setup and maintenance of the equipment. We also acknowledge Eden Paul for animal welfare including tumor measurement, mice health, and sacrificing mice. This work is supported by American Cancer Society Institutional Research Grant (IRG-58-009-56), National Center for Advancing Translational Sciences CTSA award, and CDMRP Peer reviewed Cancer research program grant W81XWH1810139. XW and RB acknowledges support from National Science Foundation (NSF) grant CMMI-1634856. ODA acknowledges support by a Department of Defense, Air Force of Scientific Research, National Defense Science and Engineering Graduate (NDSEG) Fellowship, [32 CFR 168a]. RCD acknowledges supports from Vanderbilt's Trans Institutional Programs grant: Materials Durability and Environmental Research Facilities Hub (Faculty PIs - Florence Sanchez and David Kosson). MR acknowledges support from the National Institutes of Health (NIH) R00CA201304. DS and JTW acknowledges support from the NSF CBET-1554623 (JTW),

Vanderbilt Center for Immunobiology Pilot Grant, VICC Ambassador Discovery Grant, the Melanoma Research Alliance 503565, and Stand Up To Cancer Innovative Research Grant SU2C-AACR-IRG 20-17 (JTW). AEV acknowledges support from NIH (R37 CA233770-01), Breast Cancer Research Foundation (IIDRP-16-001) and Lloyd foundation of melanoma research. AR acknowledges support from NIH grant CA116021. TEM micrographs of IGN were acquired with an instrument supported by NSF EPS 1004083. TEM images of tumor and organs were acquired by using VUMC Cell Imaging Shared Resource (supported by NIH grants CA68485, DK20593, DK58404, DK59637 and EY08126).

REFERENCES

1. Bertucci, F.; Goncalves, A., Immunotherapy in Breast Cancer: the Emerging Role of PD-1 and PD-L1. *Curr. Oncol. Rep.* **2017,** *19*, 64.
2. Tumeh, P. C.; Harview, C. L.; Yearley, J. H.; Shintaku, I. P.; Taylor, E. J.; Robert, L.; Chmielowski, B.; Spasic, M.; Henry, G.; Ciobanu, V.; West, A. N.; Carmona, M.; Kivork, C.; Seja, E.; Cherry, G.; Gutierrez, A. J.; Grogan, T. R.; Mateus, C.; Tomasic, G.; Glaspy, J. A.*, et al.*, PD-1 Blockade Induces Responses by Inhibiting Adaptive Immune Resistance. *Nature* **2014,** *515*, 568-571.
3. Vonderheide, R. H.; Domchek, S. M.; Clark, A. S., Immunotherapy for Breast Cancer: What Are We Missing? *Clin. Cancer Res.* **2017,** *23*, 2640-2646.
4. Jenkins, R. W.; Barbie, D. A.; Flaherty, K. T., Mechanisms of Resistance to Immune Checkpoint Inhibitors. *Br. J. Cancer* **2018,** *118*, 9-16.
5. Liang, Y.; Tang, H.; Guo, J.; Qiu, X.; Yang, Z.; Ren, Z.; Sun, Z.; Bian, Y.; Xu, L.; Xu, H.; Shen, J.; Han, Y.; Dong, H.; Peng, H.; Fu, Y.-X., Targeting IFNα to Tumor by Anti-PD-L1 Creates Feedforward Antitumor Responses to Overcome Checkpoint Blockade Resistance. *Nat. Commun.* **2018,** *9*, 4586.
6. Rasmussen, J. H.; Lelkaitis, G.; Håkansson, K.; Vogelius, I. R.; Johannesen, H. H.; Fischer, B. M.; Bentzen, S. M.; Specht, L.; Kristensen, C. A.; von Buchwald, C.; Wessel, I.; Friborg, J., Intratumor Heterogeneity of PD-L1 Expression in Head and Neck Squamous Cell Carcinoma. *Br. J. Cancer* **2019,** *120*, 1003-1006.
7. Gniadek, T. J.; Li, Q. K.; Tully, E.; Chatterjee, S.; Nimmagadda, S.; Gabrielson, E., Heterogeneous Expression of PD-L1 in Pulmonary Squamous Cell Carcinoma and Adenocarcinoma: Implications for Assessment by Small Biopsy. *Mod. Pathol.* **2017,** *30*, 530-538.
8. Nishino, M.; Ramaiya, N. H.; Hatabu, H.; Hodi, F. S., Monitoring Immune-Checkpoint Blockade: Response Evaluation and Biomarker Development. *Nat. Rev. Clin. Oncol.* **2017,** *14*, 655-668.

9. Broos, K.; Lecocq, Q.; Raes, G.; Devoogdt, N.; Keyaerts, M.; Breckpot, K., Noninvasive Imaging of the PD-1:PD-L1 Immune Checkpoint: Embracing Nuclear Medicine for the Benefit of Personalized Immunotherapy. *Theranostics* **2018,** *8*, 3559-3570.
10. Fumet, J.-D.; Richard, C.; Ledys, F.; Klopfenstein, Q.; Joubert, P.; Routy, B.; Truntzer, C.; Gagné, A.; Hamel, M.-A.; Guimaraes, C. F.; Coudert, B.; Arnould, L.; Favier, L.; Lagrange, A.; Ladoire, S.; Saintigny, P.; Ortiz-Cuaran, S.; Perol, M.; Foucher, P.; Hofman, P.*, et al.*, Prognostic and Predictive Role of CD8 and PD-L1 Determination in Lung Tumor Tissue of Patients Under Anti-PD-1 Therapy. *Br. J. Cancer* **2018,** *119*, 950-960.
11. Hamanishi, J.; Mandai, M.; Iwasaki, M.; Okazaki, T.; Tanaka, Y.; Yamaguchi, K.; Higuchi, T.; Yagi, H.; Takakura, K.; Minato, N.; Honjo, T.; Fujii, S., Programmed Cell Death 1 Ligand 1 and Tumor-Infiltrating CD8+ T Lymphocytes Are Prognostic Factors of Human Ovarian Cancer. *Proc. Natl. Acad. Sci. U.S.A.* **2007,** *104*, 3360-3365.
12. Huang, A. C.; Postow, M. A.; Orlowski, R. J.; Mick, R.; Bengsch, B.; Sasikanth Manne; Xu, W.; Harmon, S.; Giles, J. R.; Wenz, B.; Adamow, M.; Kuk, D.; Panageas, K. S.; Carrera, C.; Wong, P.; Quagliarello, F.; Wubbenhorst, B.; D'Andrea, K.; Pauken, K. E.; Herati, R. S.*, et al.*, T-Cell Invigoration to Tumour Burden Ratio Associated with Anti-PD-1 Response. *Nature* **2017,** *545*, 60-65.
13. Homet Moreno, B.; Zaretsky, J. M.; Garcia-Diaz, A.; Tsoi, J.; Parisi, G.; Robert, L.; Meeth, K.; Ndoye, A.; Bosenberg, M.; Weeraratna, A. T.; Graeber, T. G.; Comin-Anduix, B.; Hu-Lieskovan, S.; Ribas, A., Response to Programmed Cell Death-1 Blockade in a Murine Melanoma Syngeneic Model Requires Costimulation, CD4, and CD8 T Cells. *Cancer Immunol. Res.* **2016,** *4*, 845-857.
14. Yao, H.; Lan, J.; Li, C.; Shi, H.; Brosseau, J.-P.; Wang, H.; Lu, H.; Fang, C.; Zhang, Y.; Liang, L.; Zhou, X.; Wang, C.; Xue, Y.; Cui, Y.; Xu, J., Inhibiting PD-L1 Palmitoylation Enhances T-Cell Immune Responses Against Tumours. *Nat. Biomed. Eng.* **2019,** *3*, 306-317.
15. Kitano, A.; Ono, M.; Yoshida, M.; Noguchi, E.; Shimomura, A.; Shimoi, T.; Kodaira, M.; Yunokawa, M.; Yonemori, K.; Shimizu, C.; Kinoshita, T.; Fujiwara, Y.; Tsuda, H.; Tamura, K., Tumour-Infiltrating Lymphocytes Are Correlated With Higher Expression Levels of PD-1 and PD-L1 in Early Breast Cancer. *ESMO Open* **2017,** *2*, e000150.
16. Altan, M.; Kidwell, K. M.; Pelekanou, V.; Carvajal-Hausdorf, D. E.; Schalper, K. A.; Toki, M. I.; Thomas, D. G.; Sabel, M. S.; Hayes, D. F.; Rimm, D. L., Association of B7-H4, PD-L1, and Tumor Infiltrating Lymphocytes with Outcomes in Breast Cancer. *NPJ Breast Cancer* **2018,** *4*, 40.
17. Ding, S.-Y.; Yi, J.; Li, J.-F.; Ren, B.; Wu, D.-Y.; Panneerselvam, R.; Tian, Z.-Q., Nanostructure-Based Plasmon-Enhanced Raman Spectroscopy For Surface Analysis of Materials. *Nat. Rev. Mater.* **2016,** *1*, 16021.
18. Ou, Y.-C.; Wen, X.; Bardhan, R., Cancer Immunoimaging with Smart Nanoparticles. *Trends Biotechnol.* **2019**, https://doi.org/10.1016/j.tibtech.2019.11.001.
19. Webb, J. A.; Aufrecht, J.; Hungerford, C.; Bardhan, R., Ultrasensitive Analyte Detection with Plasmonic Paper Dipsticks and Swabs Integrated With Branched Nanoantennas. *J. Mater. Chem. C* **2014,** *2*, 10446-10454.
20. Ou, Y. C.; Webb, J. A.; O'Brien, C. M.; Pence, I. J.; Lin, E. C.; Paul, E. P.; Cole, D.; Ou, S. H.; Lapierre-Landry, M.; DeLapp, R. C.; Lippmann, E. S.; Mahadevan-Jansen, A.; Bardhan, R., Diagnosis of Immunomarkers *In Vivo via* Multiplexed Surface Enhanced Raman Spectroscopy with Gold Nanostars. *Nanoscale* **2018,** *10*, 13092-13105.

21. Liu, J.; Blake, S. J.; Yong, M. C. R.; Harjunpää, H.; Ngiow, S. F.; Takeda, K.; Arabella Young; O'Donnell, J. S.; Allen, S.; Smyth, M. J.; Teng, M. W. L., Improved Efficacy of Neoadjuvant Compared to Adjuvant Immunotherapy to Eradicate Metastatic Disease. *Cancer Discov.* **2016,** *6*, 1382-1399.
22. Yonezawa, A.; Dutt, S.; Chester, C.; Kim, J.; Kohrt, H. E., Boosting Cancer Immunotherapy with Anti-CD137 Antibody Therapy. *Clin. Cancer Res.* **2015,** *21*, 3113-3120.
23. Ou, Y. C.; Webb, J. A.; Faley, S.; Shae, D.; Talbert, E. M.; Lin, S.; Cutright, C. C.; Wilson, J. T.; Bellan, L. M.; Bardhan, R., Gold Nanoantenna-Mediated Photothermal Drug Delivery From Thermosensitive Liposomes in Breast Cancer. *ACS Omega* **2016,** *1*, 234-243.
24. Webb, J. A.; Erwin, W. R.; Zarick, H. F.; Aufrecht, J.; Manning, H. W.; Lang, M. J.; Pint, C. L.; Bardhan, R., Geometry-Dependent Plasmonic Tunability and Photothermal Characteristics of Multibranched Gold Nanoantennas. *J. Phys. Chem. C* **2014,** *118*, 3696-3707.
25. Tamura, K.; Kurihara, H.; Yonemori, K.; Tsuda, H.; Suzuki, J.; Kono, Y.; Honda, N.; Kodaira, M.; Yamamoto, H.; Yunokawa, M.; Shimizu, C.; Hasegawa, K.; Kanayama, Y.; Nozaki, S.; Kinoshita, T.; Wada, Y.; Tazawa, S.; Takahashi, K.; Watanabe, Y.; Fujiwara, Y., 64Cu-DOTA-Trastuzumab PET Imaging in Patients With HER2-Positive Breast Cancer. *J. Nucl. Med.* **2013,** *54*, 1869-1875.
26. Mortimer, J. E.; Bading, J. R.; Park, J. M.; Frankel, P. H.; Carroll, M. I.; Tran, T. T.; Poku, E. K.; Rockne, R. C.; Raubitschek, A. A.; Shively, J. E.; Colcher, D. M., Tumor Uptake of 64Cu-DOTA-Trastuzumab in Patients With Metastatic Breast Cancer. *J. Nucl. Med.* **2018,** *59*, 38-43.
27. Persson, M.; Skovgaard, D.; Brandt-Larsen, M.; Christensen, C.; Madsen, J.; Nielsen, C. H.; Thurison, T.; Klausen, T. L.; Holm, S.; Loft, A.; Berthelsen, A. K.; Ploug, M.; Pappot, H.; Brasso, K.; Kroman, N.; Højgaard, L.; Kjaer, A., First-in-Human uPAR PET: Imaging of Cancer Aggressiveness. *Theranostics* **2015,** *5*, 1303-1316.
28. Webb, J. A.; Ou, Y. C.; Faley, S.; Paul, E. P.; Hittinger, J. P.; Cutright, C. C.; Lin, E. C.; Bellan, L. M.; Bardhan, R., Theranostic Gold Nanoantennas for Simultaneous Multiplexed Raman Imaging of Immunomarkers and Photothermal Therapy. *ACS Omega* **2017,** *2*, 3583-3594.
29. Dogra, P.; Adolphi, N. L.; Wang, Z.; Lin, Y. S.; Butler, K. S.; Durfee, P. N.; Croissant, J. G.; Noureddine, A.; Coker, E. N.; Bearer, E. L.; Cristini, V.; Brinker, C. J., Establishing the Effects of Mesoporous Silica Nanoparticle Properties on *In Vivo* Disposition Using Imaging-Based Pharmacokinetics. *Nat. Commun.* **2018,** *9*, 4551.
30. Gatti, A. M.; Rivasi, F., Biocompatibility of Micro-and Nanoparticles. Part I: In Liver and Kidney. *Biomaterials* **2002,** *23*, 2381-2387.
31. Wiegand, S.; Heinen, T.; Ramaswamy, A.; Sesterhenn, A. M.; Bergemann, C.; Werner, J. A.; Lubbe, A. S., Evaluation of the Tolerance And Distribution of Intravenously Applied Ferrofluid Particles of 250 and 500 nm Size in an Animal Model. *J. Drug Target.* **2009,** *17*, 194-199.
32. Farist, F.; Thornileyt, M.; Wickramasinghet, Y.; Houstont, R.; Rolfet, P.; Livers, N.; Spencer, A., Non-Invasive *In Vivo* Near-Infrared Optical Measurement of the Penetration Depth in the Neonatal Head. *Clin. Phys. Physiol. Meas.* **1991,** *12*, 353-358.

33. Henderson, T. A.; Morries, L. D., Near-Infrared Photonic Energy Penetration: Can Infrared Phototherapy Effectively Reach the Human Brain? *Neuropsychiatr. Dis. Treat* **2015,** *11*, 2191-2208.
34. Hong, G.; Diao, S.; Chang, J.; Antaris, A. L.; Chen, C.; Zhang, B.; Zhao, S.; Atochin, D. N.; Huang, P. L.; Andreasson, K. I.; Kuo, C. J.; Dai, H., Through-Skull Fluorescence Imaging of the Brain in a New Near-Infrared Window. *Nat. Photonics* **2014,** *8*, 723-730.
35. Liu, Y.; Maccarini, P.; Palmer, G. M.; Etienne, W.; Zhao, Y.; Lee, C. T.; Ma, X.; Inman, B. A.; Vo-Dinh, T., Synergistic Immuno Photothermal Nanotherapy (SYMPHONY) for the Treatment of Unresectable and Metastatic Cancers. *Sci. Rep.* **2017,** *7*, 8606.
36. Liu, Y.; Ashton, J. R.; Moding, E. J.; Yuan, H.; Register, J. K.; Fales, A. M.; Choi, J.; Whitley, M. J.; Zhao, X.; Qi, Y.; Ma, Y.; Vaidyanathan, G.; Zalutsky, M. R.; Kirsch, D. G.; Badea, C. T.; Vo-Dinh, T., A Plasmonic Gold Nanostar Theranostic Probe for *In Vivo* Tumor Imaging and Photothermal Therapy. *Theranostics* **2015,** *5*, 946-960.
37. Meeth, K.; Wang, J. X.; Micevic, G.; Damsky, W.; Bosenberg, M. W., The YUMM Lines: A Series of Congenic Mouse Melanoma Cell Lines with Defined Genetic Alterations. *Pigment Cell Melanoma Res.* **2016,** *29*, 590-597.
38. Yang, L.; Kuang, H.; Zhang, W.; Aguilar, Z. P.; Wei, H.; Xu, H., Comparisons of the Biodistribution and Toxicological Examinations After Repeated Intravenous Administration of Silver and Gold Nanoparticles in Mice. *Sci. Rep.* **2017,** *7*, 3303.
39. Tsoi, K. M.; MacParland, S. A.; Ma, X.-Z.; Spetzler, V. N.; Echeverri, J.; Ouyang, B.; Fadel, S. M.; Sykes, E. A.; Goldaracena, N.; Kaths, J. M.; Conneely, J. B.; Alman, B. A.; Selzner, M.; Ostrowski, M. A.; Adeyi, O. A.; Zilman, A.; McGilvray, I. D.; Chan, W. C. W., Mechanism of Hard-Nanomaterial Clearance by the Liver. *Nat. Mater.* **2016,** *15*, 1212-1221.
40. Park, S.-m.; Aalipour, A.; Vermesh, O.; Yu, J. H.; Gambhir, S. S., Towards Clinically Translatable *In Vivo* Nanodiagnostics. *Nat. Rev. Mater.* **2017,** *2*, 17014.
41. Bensch, F.; van der Veen, E. L.; Lub-de Hooge, M. N.; Jorritsma-Smit, A.; Boellaard, R.; Kok, I. C.; Oosting, S. F.; Schröder, C. P.; Hiltermann, T. J. N.; van der Wekken, A. J.; Groen, H. J. M.; Kwee, T. C.; Elias, S. G.; Gietema, J. A.; Bohorquez, S. S.; de Crespigny, A.; Williams, S.-P.; Mancao, C.; Brouwers, A. H.; Fine, B. M.*, et al.*, 89Zr-Atezolizumab Imaging as a Non-Invasive Approach to Assess Clinical Response to PD-L1 Blockade in Cancer. *Nat. Med.* **2018,** *24*, 1852-1858.
42. Tavaré, R.; Escuin-Ordinas, H.; Mok, S.; McCracken, M. N.; Zettlitz, K. A.; Salazar, F. B.; Witte, O. N.; Ribas, A.; Wu, A. M., An Effective Immuno-PET Imaging Method to Monitor CD8-Dependent Responses to Immunotherapy. *Cancer Res.* **2016,** *76*, 73-82.
43. Jiang, L.; Tu, Y.; Hu, X.; Bao, A.; Chen, H.; Ma, X.; Doyle, T.; Shi, H.; Cheng, Z., Pilot Study of 64Cu(I) for PET Imaging of Melanoma. *Sci. Rep.* **2017,** *7*, 2574.
44. Sprague, J. E.; Peng, Y.; Sun, X.; Weisman, G. R.; Wong, E. H.; Achilefu, S.; Anderson, C. J., Preparation and Biological Evaluation of Copper-64–Labeled Tyr3-Octreotate Using a Cross-Bridged Macrocyclic Chelator. *Clin. Cancer Res.* **2004,** *10*, 8674-8682.
45. Sato, Y.; Oh, M.; Mori, T.; Kiyono, Y.; Fujieda, S.; Okazawa, H., Tumor-to-Muscle Ratio of Cu-ATSM Uptake May Reflect Outcome of Treatment in Head-and-Neck Cancers. *J. Nucl. Med.* **2013,** *54*, 1526-1526.
46. Fleming, I. N.; Manavaki, R.; Blower, P. J.; West, C.; Williams, K. J.; Harris, A. L.; Domarkas, J.; Lord, S.; Baldry, C.; Gilbert, F. J., Imaging Tumour Hypoxia with Positron Emission Tomography. *Br. J. Cancer* **2015,** *112*, 238-250.

47. Ping Li, W.; Meyer, L. A.; Capretto, D. A.; Sherman, C. D.; Anderson, C. J., Receptor-Binding, Biodistribution, and Metabolism Studies of 64Cu-DOTA-Cetuximab, a PET-Imaging Agent for Epidermal Growth-Factor Receptor-Positive Tumors. *Cancer Biother. Radiopharm.* **2008,** *23*, 158-171.
48. Hettich, M.; Braun, F.; Bartholoma, M. D.; Schirmbeck, R.; Niedermann, G., High-Resolution PET Imaging with Therapeutic Antibody-Based PD-1/PD-L1 Checkpoint Tracers. *Theranostics* **2016,** *6*, 1629-1640.
49. Lee, H.; Shields, A. F.; Siegel, B. A.; Miller, K. D.; Krop, I.; Ma, C. X.; LoRusso, P. M.; Munster, P. N.; Campbell, K.; Gaddy, D. F.; Leonard, S. C.; Geretti, E.; Blocker, S. J.; Kirpotin, D. B.; Moyo, V.; Wickham, T. J.; Hendriks, B. S., (64)Cu-MM-302 Positron Emission Tomography Quantifies Variability of Enhanced Permeability and Retention of Nanoparticles in Relation to Treatment Response in Patients with Metastatic Breast Cancer. *Clin. Cancer Res.* **2017,** *23*, 4190-4202.
50. Lieber, C. A.; Majumder, S. K.; Ellis, D. L.; Billheimer, D. D.; Mahadevan-Jansen, A., *In Vivo* Nonmelanoma Skin Cancer Diagnosis Using Raman Microspectroscopy. *Lasers Surg. Med.* **2008,** *40*, 461-467.
51. Movasaghi, Z.; Rehman, S.; Rehman, I. U., Raman Spectroscopy of Biological Tissues. *Appl. Spectrosc. Rev.* **2007,** *42*, 493-541.
52. Wilhelm, S.; Tavares, A. J.; Dai, Q.; Ohta, S.; Audet, J.; Dvorak, H. F.; Chan, W. C. W., Analysis of Nanoparticle Delivery to Tumours. *Nat. Rev. Mater.* **2016,** *1*, 16014.
53. Cohen, J. V.; Alomari, A. K.; Vortmeyer, A. O.; Jilaveanu, L. B.; Goldberg, S. B.; Mahajan, A.; Chiang, V. L.; Kluger, H. M., Melanoma Brain Metastasis Pseudoprogression After Pembrolizumab Treatment. *Cancer Immunol. Res.* **2016,** *4*, 179-182.
54. Gerwing, M.; Herrmann, K.; Helfen, A.; Schliemann, C.; Berdel, W. E.; Eisenblätter, M.; Wildgruber, M., The Beginning of the End for Conventional RECIST — Novel Therapies Require Novel Imaging Approaches. *Nat. Rev. Clin. Oncol.* **2019,** *16*, 442-458.
55. Cheng, L.; Lopez-Beltran, A.; Massari, F.; MacLennan, G. T.; Montironi, R., Molecular Testing for BRAF Mutations to Inform Melanoma Treatment Decisions: A Move Toward Precision Medicine. *Mod. Pathol.* **2018,** *31*, 24-38.
56. Munoz-Couselo, E.; Adelantado, E. Z.; Ortiz, C.; Garcia, J. S.; Perez-Garcia, J., NRAS-Mutant Melanoma: Current Challenges and Future Prospect. *Onco. Targets Ther.* **2017,** *10*, 3941-3947.
57. Rastinehad, A. R.; Anastos, H.; Wajswol, E.; Winoker, J. S.; Sfakianos, J. P.; Doppalapudi, S. K.; Carrick, M. R.; Knauer, C. J.; Taouli, B.; Lewis, S. C.; Tewari, A. K.; Schwartz, J. A.; Canfield, S. E.; George, A. K.; West, J. L.; Halas, N. J., Gold Nanoshell-Localized Photothermal Ablation of Prostate Tumors in a Clinical Pilot Device Study. *Proc. Natl. Acad. Sci. U.S.A.* **2019,** *116*, 18590-18596.
58. Ku, G.; Wang, L. V., Deeply Penetrating Photoacoustic Tomography in Biological Tissues Enhanced with an Optical Contrast Agent. *Optics Letters* **2005,** *30*, 507-509.
59. Lyng, F. M.; Traynor, D.; Nguyen, T. N. Q.; Meade, A. D.; Rakib, F.; Al-Saady, R.; Goormaghtigh, E.; Al-Saad, K.; Ali, M. H., Discrimination of Breast Cancer from Benign Tumours Using Raman Spectroscopy. *PLoS ONE* **2019,** *14*, e0216311.
60. Jermyn, M.; Mok, K.; Mercier, J.; Desroches, J.; Pichette, J.; Saint-Arnaud, K.; Bernstein, L.; Guiot, M.-C.; Petrecca, K.; Leblond, F., Intraoperative Brain Cancer Detection with Raman Spectroscopy in Humans. *Science Trans. Med.* **2015,** *7*, 274ra19.

61. Andreou, C.; Neuschmelting, V.; Tschaharganeh, D.-F.; Huang, C.-H.; Oseledchyk, A.; Iacono, P.; Karabeber, H.; Colen, R. R.; Mannelli, L.; Lowe, S. W.; Kircher, M. F., Imaging of Liver Tumors Using Surface-Enhanced Raman Scattering Nanoparticles. *ACS Nano* **2016,** *10*, 5015−5026.
62. Liang, W.; Hall, G.; Messerschmidt, B.; Li, M.-J.; Li, X., Nonlinear Optical Endomicroscopy for Label-Free Functional Histology *In Vivo*. *Light: Sci. App.* **2017,** *6*, e17082.
63. Pisanello, F.; LeonardoSileo; A.Oldenburg, I.; MarcoPisanello; LuigiMartiradonna; A.Assad, J.; L.Sabatini, B.; Vittorio, M., Multipoint-Emitting Optical Fibers for Spatially Addressable *In Vivo* Optogenetics. *Neuron* **2014,** *82*, 1245-1254.
64. Harmsen, S.; Wall, M. A.; Huang, R.; Kircher, M. F., Cancer Imaging Using Surface-Enhanced Resonance Raman Scattering Nanoparticles. *Nat. Protoc.* **2017,** *12*, 1400-1414.
65. Laing, S.; Jamieson, L. E.; Faulds, K.; Graham, D., Surface-Enhanced Raman Spectroscopy for *In Vivo* Biosensing. *Nat. Rev. Chem.* **2017,** *1*, 0060.
66. Schindelin, J.; Arganda-Carreras, I.; Frise, E.; Kaynig, V.; Longair, M.; Pietzsch, T.; Preibisch, S.; Rueden, C.; Saalfeld, S.; Schmid, B., Fiji: An Open-Source Platform for Biological-Image Analysis. *Nat. Methods* **2012,** *9*, 676-682.

TOC